

# Scale Size Estimation ~~of~~ and Flow Pattern Recognition around a Magnetosheath ~~Jets~~Jet

Adrian Pöppelwerth<sup>1</sup>, Georg Glebe<sup>1,2</sup>, Johannes Z. D. Mieth<sup>1</sup>, Florian Koller<sup>3</sup>, Tomas Karlsson<sup>4</sup>, Zoltan Vörös<sup>5,6</sup>, and Ferdinand Plaschke<sup>1</sup>

<sup>1</sup>Institute of Geophysics and Extraterrestrial Physics, Technische Universität Braunschweig, Braunschweig, Germany

<sup>2</sup>School of Earth and Atmospheric Sciences, Georgia Institute of Technology, Atlanta, Georgia, USA

<sup>3</sup>Institute of Physics, University of Graz, Graz, Austria

<sup>4</sup>Division of Space and Plasma Physics, School of Electrical Engineering and Computer Science, KTH Royal Institute of Technology, Stockholm, Sweden

<sup>5</sup>Space Research Institute, Austrian Academy of Sciences, Graz, Austria

<sup>6</sup>Institute of Earth Physics and Space Science, HUN-REN, Sopron, Hungary

**Correspondence:** Adrian Pöppelwerth (a.poeppelwerth@tu-braunschweig.de)

**Abstract.** Transient enhancements in the dynamic pressure, so-called magnetosheath jets or simply jets, are abundantly found in the magnetosheath. ~~After their formation at~~ They travel from the bow shock ~~, they travel~~ through the magnetosheath towards the magnetopause. On their way through the magnetosheath, jets disturb the ambient plasma. Multiple studies already investigated their scale size perpendicular to their propagation direction, and almost exclusively in a statistical manner. In this paper, we use multi-point measurements from the Time History of Events and Macroscale Interactions during Substorms (THEMIS) mission ~~of the motion of ambient magnetosheath plasma responding to~~ to study the passage of a ~~jet to reconstruct the location~~ single jet. We observe an vortical motion of the plasma on the jet path. Using this passage we can reconstruct the position of the central axis of ~~that jet,~~ this jet along its propagation direction. This method allows us to estimate the spatial distribution of the dynamic pressure within the jet. ~~In addition, the scale~~ Furthermore, the size perpendicular to the propagation direction ~~could~~ can be estimated for different cross sections. ~~Both~~ Using this method, the scale size of individual jet events can be determined with multiple spacecraft. In principle, only two spacecraft are needed if we assume a simplified geometry and stationarity of the jet during the observation.

In the jet event investigated here, both the dynamic pressure and ~~scale size decrease from the center~~ the perpendicular size increase along the propagation axis ~~towards the~~ from the front part towards the center of the jet and decrease again towards the rear part. We obtain a maximum diameter in the perpendicular direction of about  $1 R_E$  and a dynamic pressure of about 6 nPa at the jet center.

## 1 Introduction

The magnetic field of the Earth is an obstacle to the supersonic solar wind. To flow around the magnetopause, the boundary between the terrestrial and interplanetary magnetic fields (IMF), the solar wind must be decelerated to sub-magnetosonic speeds. This takes place upstream at the bow shock where the solar wind is decelerated, heated and deflected.

Depending on the angle  $\theta - \theta_{\text{BN}}$  between the bow shock normal and the IMF, the bow shock can be divided into a quasi-parallel ( $\theta < 45^\circ$  or  $\theta_{\text{BN}} < 45^\circ$ ) or quasi-perpendicular ( $\theta > 45^\circ$  or  $\theta_{\text{BN}} > 45^\circ$ ) shock (e.g., Balogh et al., 2005). Particles reflected at the quasi-parallel shock can travel far upstream along the IMF and interact with the incoming solar wind. This leads to a region called foreshock which hosts a zoo of instabilities and waves (Eastwood et al., 2005). The waves are convected back to the shock with the solar wind, causing a rippled and undulated quasi-parallel bow shock.

The region between the bow shock and the magnetopause is called magnetosheath (e.g., Spreiter et al., 1966). In the magnetosheath, localized enhancements in the dynamic pressure are frequently observed. These so-called magnetosheath jets (see the review by Plaschke et al., 2018) were first reported by Němeček et al. (1998). ~~They~~ Various definitions of jets can be found in the literature, which compare the dynamic pressure enhancement e.g. with the ambient plasma (e.g. Archer et al., 2012) or with the upstream solar wind (e.g. Plaschke et al., 2013). Jets are observed more often behind the quasi-parallel bow shock (e.g., Vuorinen et al., 2019) which corresponds to low IMF cone angle conditions for the subsolar magnetosheath and favor quiet solar wind (e.g., Plaschke et al., 2013). LaMoury et al. (2021) and Koller et al. (2023) further investigated the statistical dependence of jet occurrence ~~from on~~ solar wind parameters. Jet impact rates determined by LaMoury et al. (2021) showed that more magnetosheath jets impact the magnetopause during low IMF magnitude, low solar wind density and high Mach number conditions. However, the dominant occurrence controlling parameters are low IMF cone angles and high solar wind speeds.

Jet formation downstream of the quasi-parallel bow shock may be explained by a mechanism suggested by Hietala et al. (2009, 2012). At the undulated bow shock, the incoming solar wind will be less decelerated and heated when passing the inclined parts. The geometry of the ripples can cause the flow to converge or diverge, resulting in density increases or decreases behind the shock. This leads to plasma regions with higher velocity and density than in the surrounding magnetosheath. Jets may also form due to solar wind discontinuities interacting with the bow shock (e.g., Archer et al., 2012). For example, Hot Flow Anomalies (HFAs, e.g. Savin et al., 2012) or short large amplitude magnetic structures (SLAMS, e.g. Schwartz and Burgess, 1991) can cause additional shock rippling when passing through the shock (e.g., Karlsson et al., 2018; Raptis et al., 2022b). That was also visible in simulations by Suni et al. (2021). They showed that jets can form due to the impact of compressional structures (like SLAMS) at the bow shock, ~~without the detour with the shock ripple approach.~~

Geoeffective jets (with diameters  $> 2R_E$ ) reach the magnetopause several times per hour (Plaschke et al., 2020a) and have therefore a big impact on the magnetosphere and ionosphere. They can indent the magnetopause (e.g., Shue et al., 2009), cause surface waves (e.g., Archer et al., 2019) and may even penetrate through the boundary (e.g., Dmitriev and Suvorova, 2015). Hietala et al. (2018) showed that jets can trigger and suppress reconnection at the magnetopause, ~~as they can modify~~ the magnetic field in the magnetosheath and thus alter the shear angle at the magnetopause. This leads to situations where reconnection is triggered when it is not expected and vice versa (see also Vuorinen et al., 2021). Additionally, upon impact, jets can enhance ionospheric flow channels (Hietala et al., 2012) and disturb radio communication (Dmitriev and Suvorova, 2023). Nykyri et al. (2019) proposed ~~for a single event~~ that jets might even trigger substorms, leading to auroral brightenings. Also, Han et al. (2017) hypothesized in a statistical study that jets impacting the magnetopause are one possible source of throat auroras.

On their way from the bow shock to the magnetopause, plasma jets interact with the ambient magnetosheath plasma. Palmroth et al. (2021) used global hybrid-Vlasov simulations to study the evolution of jets inside the magnetosheath. They reported that the jets thermalize on their way to the magnetopause and become more 'magnetosheath-like' while they keep their propagation direction. In addition Raptis et al. (2022a) reported that jets may contain two plasma populations, a cold and fast jet and a hotter and slower background population. Not only the jets but also the ambient plasma is affected from the interaction. Recent studies showed a slight alignment of the magnetic field ~~lines~~ along the jet propagation direction (Plaschke et al., 2020b) and a stirring of the magnetosheath plasma in the vicinity of the jet (Plaschke et al., 2017). Plaschke and Hietala (2018) reported in a statistical analysis ~~of several hundred jets that they that jets~~ push slower plasma ahead of them and out of their way. Jets act like plows, and after their passage, the magnetosheath plasma fills the wake regions behind them. ~~They~~ Plaschke and Hietala (2018) speculated that properties of jets like their scale size may influence the interaction.

Multiple studies report that magnetosheath jets have scale sizes ~~on-in~~ the order of  $1 R_E$  in the directions parallel and perpendicular to the jet propagation. To obtain a simple estimation of the parallel size of a jet, it is sufficient to integrate the plasma velocity over the jet observation interval (Plaschke et al., 2020a) or multiply the duration of the jet interval with the maximum speed to get an upper size limit (Gunell et al., 2014). To obtain the perpendicular size at least two spacecraft are needed. Plaschke et al. (2016, 2020a) and Gunell et al. (2014) used pairs of spacecraft and derived the scale sizes in statistical studies from the probabilities for both spacecraft to observe a jet. Karlsson et al. (2012) used the four Cluster spacecraft (Escoubet et al., 2001) to investigate the scale sizes of single jets. The authors performed a minimum variance analysis to obtain a suitable, jet specific coordinate system. They extrapolated density profiles along these directions with linear fits allowing them to estimate the scale sizes in all 3 directions.

However, apart from Karlsson et al. (2012), all aforementioned authors used statistical analyses to obtain information on the scale sizes and other properties of magnetosheath jets. Here we show for the first time the spatial distribution of the dynamic pressure within different cross sections of a jet. Therefore To achieve this, we select a jet event observed by the Time History of Events and Macroscale Interactions during Substorms (THEMIS) spacecraft (Angelopoulos, 2008) ~~to determine the central axis of this jet from the evasive motion of the ambient plasma~~ and transform the velocity measurements in to a coordinate system aligned with the jet propagation direction. We use the vortical behavior of the plasma in the jet path (Plaschke and Hietala, 2018) to determine the position of the spacecraft within the plane perpendicular to the propagation direction. Ultimately, we use the positions and measurements of the spacecraft to estimate dynamic pressure profiles perpendicular to the propagation direction within different cross sections. In addition, we determine the perpendicular sizes with these profiles for different cross sections.

## 85 2 Data and Methods

We focus on a jet observed by the THEMIS A, D, and E spacecraft (THA, THD, THE) on 13 October 2010, around 16:04:00 UT. Measurements of the magnetic field (FGM, Auster et al., 2008), ion velocity, ion density, ion energy flux density and dynamic pressure (ESA, McFadden et al., 2008) in the GSE-X direction ( $P_{\text{dyn},x}$ ) are shown in Fig. 1 ~~(all in spin fit in the rows~~

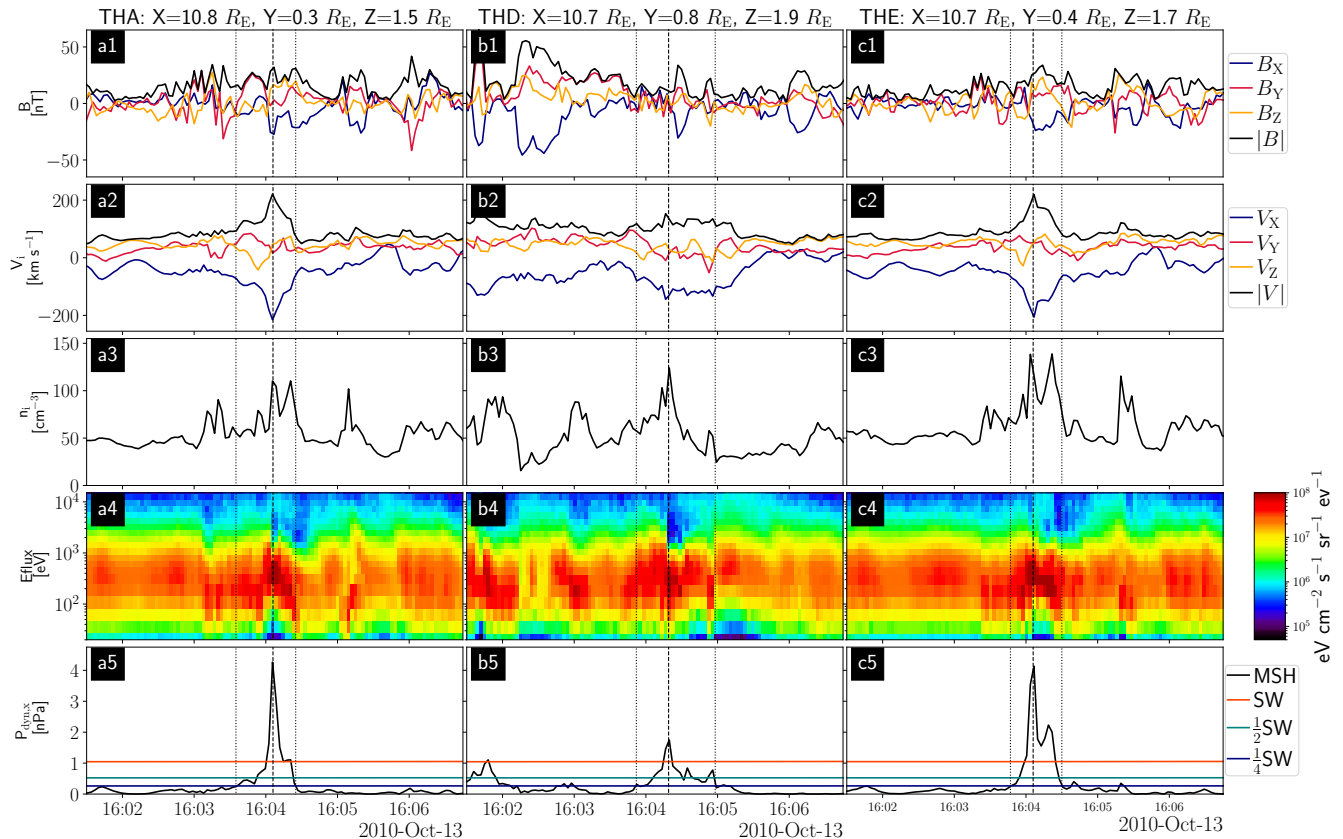


**Figure 1.** Plasma jet observed by the three THEMIS spacecraft THA (a), THD (b), and THE (c), respectively. From top to bottom, the magnetic field and ion velocity components in GSE coordinates and their magnitudes, the ion density, the ion energy flux density, and the GSE-X component of the dynamic pressure are shown. The vertical dashed lines in each column mark the times of maximum dynamic pressure ratio ( $t_{\max}$ ). The dotted lines denote the start ( $t_{\text{start}}$ ) and end times ( $t_{\text{end}}$ ) of the jet intervals. The horizontal lines in the last row represent the solar wind dynamic pressure, as well as half and a quarter thereof (in orange, cyan, and blue, respectively).

from top to bottom (full moments in spin resolution). Following Plaschke et al. (2013), we label the point of maximum dynamic pressure ratio with reference to upstream OMNI the upstream OMNI solar wind measurements (King and Papitashvili, 2005) as  $t_{\max}$ . Start and end times of the jet interval are labeled as  $t_{\text{start}}$  and  $t_{\text{end}}$ , respectively. They denote the times where  $P_{\text{dyn},x}$  equal one quarter of the solar wind dynamic pressure ( $P_{\text{dyn},\text{sw}}$ ). The spacecraft THA, THD and THE observed the jet for 50s, 66s and 43s, 50 s, 66 s and 43 s, respectively.

The rows show from top to bottom, the magnetic field and ion velocity components in GSE coordinates and their magnitudes, the ion density, the ion energy flux density, and the GSE-X component of the dynamic pressure. The ion energy flux density (Fig. 1a4-c4) together with the high ion density (Fig. 1a3-c3) clearly shows that all three spacecraft are in the magnetosheath at the time of the event. The positions in GSE coordinates are given above each column of the figure; they show

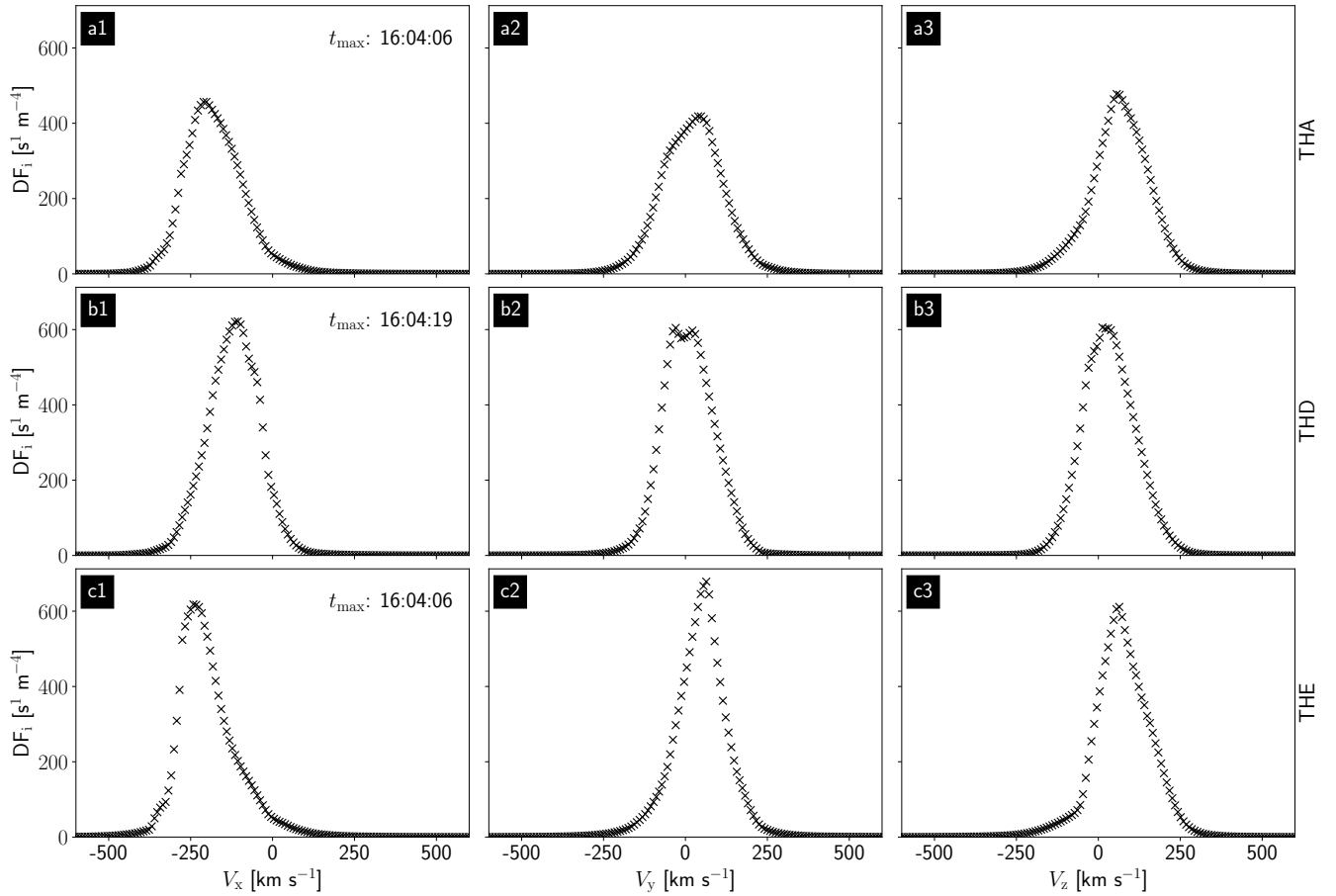


**Figure 2.** [The integrated 1D velocity distribution function along the velocity components at the time of maximum dynamic pressure  \$t\_{\max}\$ . The columns from left to right represent the  \$V\_x\$ ,  \$V\_y\$  and  \$V\_z\$  component, respectively. The rows from top to bottom show the results for THA, THD and THE, respectively. In the left column we denote the time  \$t\_{\max}\$  for each spacecraft.](#)

that all spacecraft are close to the sun-earth line. The dynamic pressure (Fig. 1a5-c5) exhibits [for all spacecraft](#) a clear increase above the solar wind value [for all spacecraft](#), ensuring that we are indeed observing a jet. The times  $t_{\max}$  are separated by only [13s-13 s](#) and the dynamic pressure peaks resulted from a combined increase in ion density and  $V_x$  for every spacecraft.

[Raptis et al. \(2022a\)](#) have shown by investigating the velocity distribution function (VDF) that jets may contain a mixture of two plasma populations. In a similar manner we integrated the 3D VDF over two velocity axes to obtain a 1D VDF along the third velocity component. This is shown in Fig. 2 for time  $t_{\max}$  for all three velocity components of THA, THD and THE.

[We notice in agreement with Raptis et al. \(2022a\)](#) that the  $V_y$  component (VDF) of THD (see Fig. 2b2) shows two separate maxima. THA and THE measurements exhibit only single peaks in the 1D VDFs, but deviate from the ideal Maxwellian distribution (see Fig. 2a1-a3 and c1-c3). As THD is further away from the other two spacecraft and observes a lower dynamic pressure, we assume THD to be closer to the edge of the jet. The two maxima could indicate that THD is observing a mixture of

jet and magnetosheath plasmas. Therefore, we continue our analysis only considering THA and THE, using the peak velocities in the 1D VDFs.

110 To facilitate the analysis of the measurements, we need to define a coordinate system that is aligned with the direction of the jet propagation direction and in the rest frame of the ambient magnetosheath plasma. The axes of the new coordinate system are given as follows:-

$$\underline{\underline{X'}} = \frac{V_{\text{Jet}} - \langle V_{\text{MSH}} \rangle_{15\text{min}}}{|V_{\text{Jet}} - \langle V_{\text{MSH}} \rangle_{15\text{min}}|}, \quad \underline{\underline{Y'}} = \frac{X' \times \hat{X}}{|X' \times \hat{X}|}, \quad \underline{\underline{Z'}} = \frac{X' \times Y'}{|X' \times Y'|}.$$

115 For simplicity, As apparent in Fig. 1 the velocities are rather turbulent. Therefore, we choose  $\langle V_{\text{MSH}} \rangle_{15\text{min}}$  to be the mean velocity measured by all three spacecraft in a 15min window around  $t_{\text{max}}$ .  $V_{\text{Jet}}$  is the mean velocity measured by all three spacecraft at their respective a short time (12 s) centered around  $t_{\text{max}}$  times and investigated the velocity directions measured by THA and THE to determine the propagation direction. For an easier comparison of the directions we use spherical coordinates with the polar angle  $\Theta$  and the azimuthal angle  $\varphi$  to visualize the direction of the velocities:

$$\Theta = \arccos\left(\frac{z}{\sqrt{x^2 + y^2 + z^2}}\right), \quad \varphi = \text{sgn}(y) \cdot \arccos\left(\frac{x}{\sqrt{x^2 + y^2}}\right). \quad (1)$$

120 The results are shown in Fig. 3 where the crosses in red, orange and blue represent the measurements of THA, THD and THE, respectively. THD is deviating strongly from THA and THE and is only shown for completeness. The black dot represents the mean value of the THA and THE measurements.

The directions of THA and THE are more similar and variate not to much around  $t_{\text{max}}$ . We therefore can assume that the mean values of  $\Theta = 73.05^\circ$  and  $\varphi = 163.18^\circ$  represent the propagation direction  $V_{\text{jet}}$  well. In addition, we also calculate the standard deviation ( $\Theta = 4.04^\circ, \varphi = 4.48^\circ$ ) and maximum difference from the mean ( $\Theta = 7.63^\circ, \varphi = 9.00^\circ$ ). To treat the uncertainty of the propagation direction conservatively, we will use the maximum differences as error estimation. With the mean values for  $\Theta$  and  $\varphi$  we determine the propagation direction  $V_{\text{jet}} = [-0.92, 0.28, 0.29]$  (in GSE coordinates) and calculate the axes of the new coordinate system as follows:

$$\underline{\underline{X'}} = V_{\text{jet}}, \quad \underline{\underline{Y'}} = \frac{X' \times \hat{X}}{|X' \times \hat{X}|}, \quad \underline{\underline{Z'}} = \frac{X' \times Y'}{|X' \times Y'|}. \quad (2)$$

130  $\hat{X}$  is the unit vector along the GSE-X axis.  $X'$  points in the propagation direction of the jet in the ambient plasma rest frame, while  $Y'$  and  $Z'$  are oriented perpendicular to the propagation direction and complete the right handed system. We shift the time-series of velocities and positions of THA and THE by 13s each so that all spacecraft observe  $t_{\text{max}}$  at the same time. We subtract  $\langle V_{\text{MSH}} \rangle_{15\text{min}}$  from the measured ion velocities and then transform choose the position of spacecraft THA at  $t_{\text{max}}$  (see Fig. 1) as origin of our jet coordinate system since THA observes the highest dynamic pressure. To transform the velocities and positions we simply rotate them into the new coordinate system. The spacecraft positions are transformed directly into the new coordinate system. Measured ion velocity, time-averaged over the neighboring data points, at the three spacecraft positions

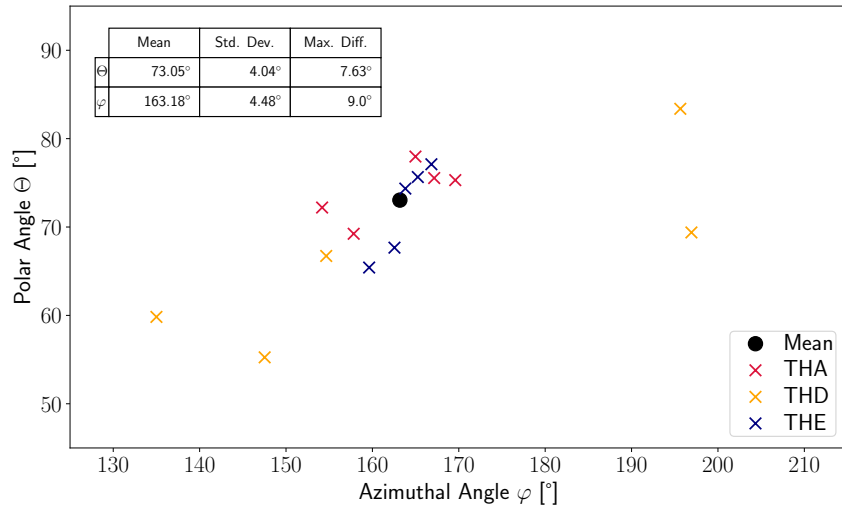


**Figure 3.** The polar angle  $\Theta$  plotted against the azimuthal angle  $\varphi$  for velocity measurements of THA, THD and THE around  $t_{\max}$  in red, orange and blue, respectively. The black dot represents the mean value of the THA and THE measurements. The table in the upper right shows the mean values, standard deviations and maximum differences of  $\Theta$  and  $\varphi$ .

for 9 time steps around  $t_{\max}$  in the plane perpendicular to the jet propagation direction in the magnetosheath rest frame. The circles represent the spacecraft positions and the arrows indicate the velocities. The colors for THA, THD, and THE are red, green, and blue, respectively. The black dots at each step represent the estimated center after Fig. 5. The top axis shows the corresponding  $Y'$  coordinates for each time step. The  $Z'$ -axis is the same for each time step. The bottom axis displays the time steps. In the upper left corner, the black arrow indicates the scale.

The orientations of the ion velocity vectors in the  $Y' - Z'$  plane change due to the passage of the jet. Using the jet coordinate system, we can investigate the flow patterns at the spacecraft positions. This is shown for 9 time steps from 12s before to 12s after  $t_{\max}$  in Fig. 4. The arrows indicate the ion velocities at the spacecraft positions (circles) of THA, THD and THE in red, green-orange and blue, respectively and the black dot represents the estimated center. The figure shows the orientation of the velocities in the  $Y' - Z'$  plane, perpendicular to the propagation direction, for 11 time steps from 15 s before to 15 s after  $t_{\max}$ . The  $Y'$ - and  $Z'$ -axis are identical for each time step.

Plaschke and Hietala (2018) have reported that the vortical motion of the plasma is not only visible outside of the jet after Fig. 5. but is also apparent within the jet structure. Therefore we choose this time range where all spacecraft observe the jet. We remind the reader that we will primarily focus on THA and THE as we have already discussed that THD is further away from the other two spacecraft and might observe a mixture of plasma populations. This said, we argue that the following description applies also to THD but we expect deviations from the general behavior as the conditions are different compared with THA and THE.

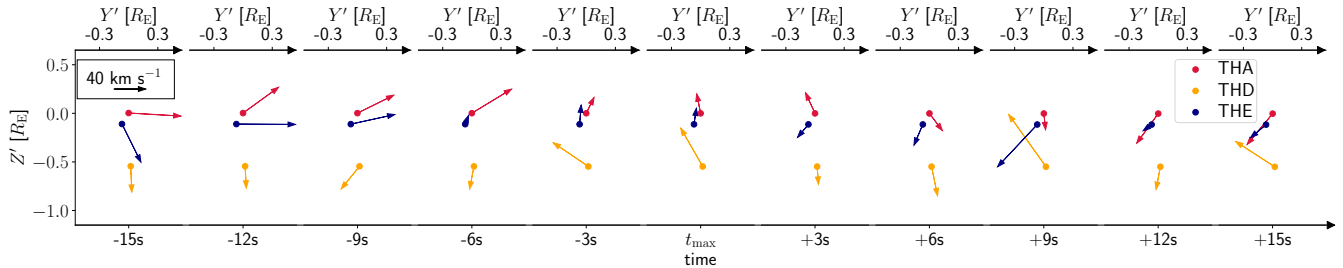


**Figure 4.** Ion velocities from the 1D VDF peaks at the three spacecraft positions for 11 time steps around  $t_{\max}$  in the plane perpendicular to the jet propagation direction. The circles represent the spacecraft positions and the arrows indicate the velocities. The colors for THA, THD, and THE are red, orange, and blue, respectively. The top axis shows the corresponding  $Y'$  coordinates for each time step, while the bottom axis displays the time steps. In the upper left corner, the black arrow indicates the scale.

On the left side of the figure Fig. 4, prior to jet passage  $t_{\max}$ , the arrows point in different directions. While the velocities at THA and THE point in the towards the positive  $Y'$  direction (away from the jet center), at THD the velocity is directed in the opposite direction, but in different  $Z'$  directions. We interpret this as signs of diverging flow. Closer to  $t_{\max}$ , from 3 s before to 9 s after  $t_{\max}$ , the arrows show a diverging pattern with THA pointing in the positive and THE in the negative  $Z'$  direction. The arrow at THD starts to rotate clockwise and points away from the center. Directly in front of  $t_{\max}$  the direction of the arrow at THA flips. The overall behavior before the jet passage is therefore rather complicated, rather turbulent behavior and we observe rotations of the arrows, mostly in counterclockwise direction. Looking at Fig. 1a5 and c5 we see two high dynamic pressure peaks in this time interval at THA and THE. In contrast, the arrows on the right side in Fig. 4, from -12 s to -15 s, corresponding with times after the jet passage point roughly to one point (the jet center) and visualize the  $t_{\max}$  point towards the negative  $Y'$  direction. The arrows point additionally to roughly one point and show signs of a converging plasma flows after the jet has passed the spacecraft. These observations can be interpreted as an indication of an evasive motion of the ambient plasma ahead of the jet and the subsequent filling of the wake afterwards, as reported by Plaschke and Hietala (2018).

From the wake-filling plasma flow after the jet passage observed at the three spacecraft positions, we can In Appendix A we show that the visibility of this vortical motion is not strongly dependent on the propagation direction, as the same flow patterns are still visible at THA and THE for slightly rotated coordinate systems that are consistent with the determined uncertainties.

Next we determine which regions of the jet the spacecraft observe. In order to achieve this, we use the diverging flows before and the converging flows after  $t_{\max}$  to estimate the position of the jet center. Therefore, we take a closer look at the time 9s after  $t_{\max}$  and extend the corresponding central axis of the jet. Thereafter, we can calculate the spacecraft distances from the central axis within different cross sections of the jet.

We extend the THA- and THE- velocity vectors in the  $Y'$ - $Z'$ -plane (gray lines and determine the central axis as the point where the two lines intersect. As an example, in Fig. 5). We choose this time step as the converging flow is most clearly seen here. We determine the center as the point whose perpendicular distance to all three lines is minimal. This estimation is shown in a, b we show the estimation for the time steps 12 s before and 15 s after  $t_{\max}$ . The gray lines indicate the extension of the



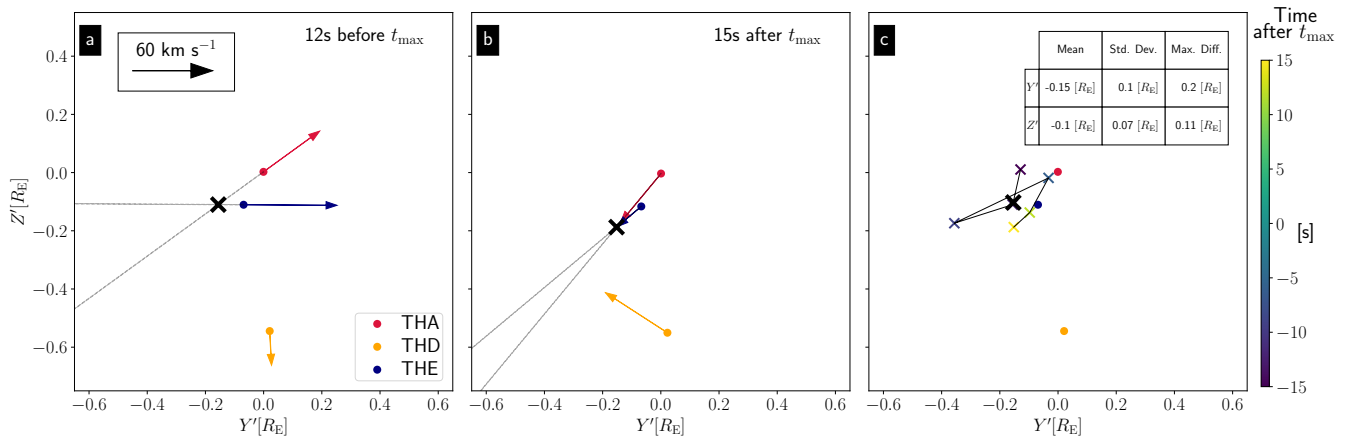


**Figure 5.** a) and b): Ion velocities from 1D VDF peaks at the three spacecraft positions 12 s before (a) and 15 s after  $t_{max}$  (b) in the plane perpendicular to the jet propagation. The circles represent the positions of the spacecraft and the arrows indicate the velocities. The colors for THA, THD, and THE are red, orange, and blue, respectively. The black arrow indicates the scale. The gray lines are simple extensions of the velocity vectors, and the black crosses mark the intersections of the lines, and representing the estimated center positions. c): The colored crosses show the estimated positions for different time steps. The color corresponds to the time as indicated by the color bar. The black cross represents the mean value and the dots in red, orange and blue are the positions of THA, THD and THE, respectively. The table in the upper right denotes the mean values, standard deviations and maximum differences of the  $Y'$  and  $Z'$  coordinates.

velocity vectors and the black cross represents the estimated position of the central axis. In Fig. 5c we present the estimated positions of the central axis for all time steps, except where we observe the largest dynamic pressures (from 3 s before to 9 s after  $t_{max}$ ).

180 Based on Fig. 5 with the black dot representing the calculated center. Due to the fact that the  $Y'$  and  $Z'$  axes are oriented perpendicular to the propagation, the c, we can calculate the mean position of the central axis:  $Y' = 0.15 R_E$  and  $Z' = 0.10 R_E$ . We also observe that the position is relatively well determined, as can be seen by the low standard deviations ( $Y' = 0.10 R_E$ ,  $Z' = 0.07 R_E$ ) and maximum differences ( $Y' = 0.20 R_E$ ,  $Z' = 0.11 R_E$ ). Only the estimation at -9 s causes a large error, especially in the  $Y'$  direction. Again, to be conservative, we use the maximum differences as uncertainties and assume the

185 position of the center in this plane should central axis to be valid for the entire jet interval, assuming a constant propagation direction. Measured ion velocity, time-averaged over the neighboring data points, at the three spacecraft positions 9s after  $t_{max}$  in the plane perpendicular to the jet propagation in the magnetosheath rest frame. The circles represent the positions of the spacecraft and the arrows indicate the velocity. The colors for THA, THD, and THE are red, green, and blue, respectively. The black arrow indicates the scale. The gray lines are simple extensions of the velocity vectors, and the black dot marks the closest

190 point to the three lines and represents the center position. The estimated center is also included in Fig. 4.

### 3 Results

~~The distances of THA, THD and THE.~~ In the next section we will use the spacecraft positions and their distances from the central axis to investigate the dynamic pressure profiles for different cross sections. In order to achieve this, we fit a Gaussian distribution that also can be used to estimate the scale size of the corresponding cross section to the  $P_{\text{dyn}}$  measurements:

$$195 \quad P_{\text{dyn,fit}} = P_0 \cdot \exp\left(\frac{-r^2}{2 \cdot \Delta R^2}\right). \quad (3)$$

Here the parameters  $P_0$  and  $\Delta R$  are the amplitude and width of the Gaussian, and  $r$  represents the distance to the center. The choice of the Gaussian profile may be somewhat arbitrary. Even though we cannot guarantee that it describes the jets in reality, the measurements in this case are well described by this profile. To apply this fit we have to assume a monotonous decrease of the dynamic pressure from the center towards the edges. We furthermore assume a rotational symmetry around the central jet axis to ensure a robust fit.

### 3 Results and Discussion

Using the estimated position of the central axis, we calculate the distances of the spacecraft from the central axis  $r$  in the  $Y'-Z'$ -plane ~~are 0.31~~. This results in distances of  $0.19 R_E$ ,  $0.54$ ~~0.48~~  $R_E$  and  $0.18$ ~~0.09~~  $R_E$  for THA, THD and THE, respectively. These values change only marginally (max. ~~53~~%) over the jet interval due to the spacecraft movement. ~~We, assuming the~~ central axis staying constant.

To obtain dynamic pressure profiles we, plot  $P_{\text{dyn},x}$  ~~as measured~~ derived from peak velocities from the 1D VDFs in the spacecraft system against these distances for different times ~~For  $t_{\text{max}}$  this is shown in and apply the Gaussian fit.~~ In Fig.6 ~~a and for we show this for the times  $t_{\text{max}} - 9$  s (a),  $t_{\text{max}}$  (b) and  $t_{\text{max}} + 12$  s it is shown in Fig. 6b. 6 s (c).~~ Crosses in red, ~~green~~~~orange~~, and blue represent the data points for THA, THD and THE, respectively. We also plot one quarter of the solar wind dynamic pressure (blue horizontal line) in Fig.6 and ~~fit a Gaussian distribution with an additional offset corresponding to the background dynamic pressure (the Gaussian distribution is shown as~~ black dashed line):-

$$P_{\text{dyn,fit}} = P_0 \cdot \exp\left(\frac{-r^2}{2 \cdot \Delta R^2}\right) + P_{\text{dyn,BG}}.$$

Here the fit parameters  $P_0$  and  $\Delta R$  give the amplitude and width of the Gaussian.  $P_{\text{dyn,BG}}$  is the background dynamic pressure in GSE-X direction and  $r$  the distance to the center. To determine  $P_{\text{dyn,BG}}$ , we average the values for  $P_{\text{dyn},x}$  measured by all three spacecraft within a 15min window around  $t_{\text{max}}$ . This results in  $P_{\text{dyn,BG}} = 0.05 \text{ nPa}$ . The intersection of the fit with  $P_{\text{dyn},x} = \frac{1}{4} P_{\text{dyn,sw}} = 0.26 \text{ nPa}$  leads to a estimation of the jet size in the direction perpendicular to the jet propagation. We choose one quarter of the solar wind dynamic pressure as a threshold to be consistent with the definition of  $t_{\text{start}}$  and  $t_{\text{end}}$  for jets, which determine the scale size along the jet propagation (see criterion of Plaschke et al., 2013). For this estimation, we assume a radially symmetric profile of the dynamic pressure around the propagation axis. The gray area visualizes the standard deviation  $\sigma$  of the optimal fit parameters. Here,  $\sigma$  is the square root of the diagonal elements of the covariance matrix for the fitting parameters.

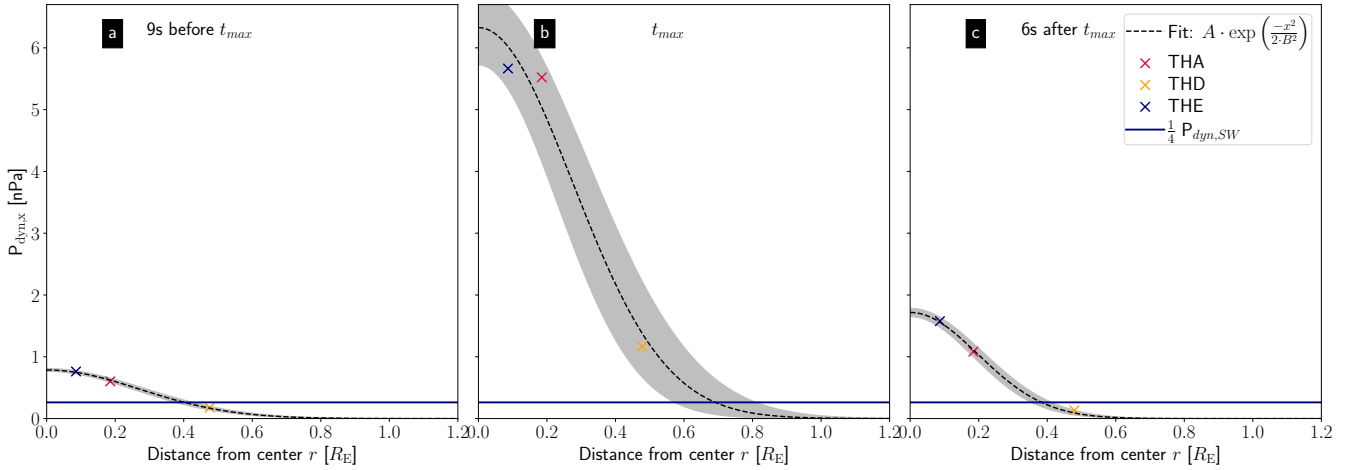


**Figure 6.** Dynamic pressure  $P_{dyn,x}$  as measured derived from velocities from the 1D VDFs in the spacecraft system versus the distance from the center  $r$  at THA, THD and THE (crosses in red, green-orange and blue, respectively) at 9 s before  $t_{max}$  (a), at  $t_{max}$  (b) and at 6 s after  $t_{max}$  (c). The black, dashed line represent a fit with a Gaussian distribution with an offset corresponding to the dynamic pressure of data points and the background magnetosheath (black) gray area visualizes when we subtract/add one standard deviation  $\sigma$  from the optimal fit parameters. The blue horizontal line depicts a quarter of the solar wind dynamic pressure.

At both times In the three time steps shown, the dynamic pressure increases towards the center. While is highest at the spacecraft closest to the center (THE). While we see some deviations from the data in Fig.6a the value at THA (further away from the center) is slightly higher than at THE (larger gray area), the fit in Fig.6b-a and c represents the data points very well.

225 The fit parameters are  $P_0 = 4.980.79 \pm 0.02$  nPa and  $\Delta R = 0.380.28 \pm 0.01$   $R_E$  for the time at  $t_{max} - 9s$ ,  $P_0 = 6.33 \pm 0.60$  nPa and  $\Delta R = 0.28 \pm 0.04$   $R_E$  at  $t_{max}$  and  $P_0 = 2.901.72 \pm 0.07$  nPa and  $\Delta R = 0.230.20 \pm 0.01$   $R_E$  for at  $t_{max} + 12s$ 6s. The estimated central jet dynamic pressure is higher at  $t_{max}$  (5nPa) than 6 nPa) than earlier at  $t_{max} - 9s$  (1 nPa) or later at  $t_{max} + 12s$  (3nPa). Therefore 6s (2 nPa). Hence, the dynamic pressure decreases-increases along the central jet axis towards the rear part of the jet from the front part towards the center of the jet and decreases afterwards towards the rear part.

230 The intersection of the fit with  $P_{dyn,x} = \frac{1}{4} P_{dyn,sw} = 0.26$  nPa leads to an estimation of the jet size in the direction perpendicular to the jet propagation. We choose one quarter of the solar wind dynamic pressure as a threshold to be consistent with the definition of  $t_{start}$  and  $t_{end}$  for jets, which determine the scale size along the jet propagation direction (see criterion of Plaschke et al., 2013). The Gaussian fits (black lines) intersect the horizontal line at 0.960.39  $R_E$  and 0.52, 0.68  $R_E$  and 0.38  $R_E$  at  $t_{max} - 9$  s,  $t_{max}$  and  $t_{max} + 12s$   $t_{max} + 6$  s, respectively. This corresponds with a larger-As the width of the Gaussian distribution  $\Delta R$  is quite similar in all three time steps, the larger (smaller) perpendicular size of the jet around  $t_{max}$  and a decrease of the size towards the rear part.

## 4 Discussion

The ideal scenario of the evasive motion of ambient plasma around a jet as described by Plaschke and Hietala (2018) consists of a clear diverging plasma flow ahead of the jet and a subsequent converging flow behind, as the ambient plasma fills the wake left by the jet. A look at Fig. 4 suggests that signs of the latter are visible; the converging plasma flow can be observed. In contrast, the diverging flow is not clearly visible. Especially for THD the flow deviates from the expectation. Additionally the velocity at THA points towards the center even slightly before ( $t_{\max}$ ). This could be the result of a more complex jet with an irregular shape associated with local turbulence generation. Alternatively a second jet may be passing by causing a complex flow pattern. The significant deviation from the average situation described by Plaschke and Hietala (2018) does not allow further interpretation of the flow pattern before  $-9$  s and  $t_{\max}$ . Nevertheless,  $+6$  s) results from the higher (lower) dynamic pressure in the jet center (front and rear parts).

We apply the fit here to the measurements from all three spacecraft to reduce the uncertainty of the parameters. In Appendix B we show that the dynamic pressure profiles do not strongly depend on the position of the converging flow after the jet passage is clearly recognizable with all arrows pointing towards the center on the right side of Fig. 4. This flow pattern allows us the determination of the jet center as shown in Fig. 5. The position of the center together with radial distances of the spacecraft lead to the estimation of the scale sizes perpendicular to the propagation direction. To verify the results obtained, we central axis, as the parameters  $P_0$  and  $\Delta R$  and their evolution over the jet interval vary only marginally with varying central axis position.

We can compare the estimated scale sizes with previous results.

In previous studies, different authors reported a range of scale sizes of magnetosheath jets. Plaschke et al. (2020a) derived that most of the jets should be on the order of  $0.1 R_E$ , although they argued that these small jets are less likely to be observed. For the observed magnetosheath jets, they report a median diameter of about  $1 R_E$  in the directions parallel and perpendicular to the flow. Gunell et al. (2014) calculated upper limits and found median values of  $4.9 R_E$  and  $3.6 R_E$  for the sizes parallel and perpendicular to the flow, respectively. Both studies used pairs of spacecraft and the probabilities that both observe a jet to calculate sizes perpendicular to the propagation directions. Karlsson et al. (2012) found scale sizes between  $0.1$  and  $10 R_E$  for one direction perpendicular to the magnetic field; for the other two dimensions the sizes were found to be a factor of 3-10 larger. Thus our results with diameters of approximately  $21.3 R_E$  at  $t_{\max}$  and  $40.8 R_E$  at times before and after  $t_{\max} +12$ s fit very well to the earlier reported sizes.

The method presented by Karlsson et al. (2012) can be used to obtain the sizes of single jet events-jets in all three dimensions. This is only possible if the structure is associated with a magnetic field discontinuity, which was the case for all their events. Contrary to this, our method provides scale sizes for the directions parallel and perpendicular to the flow under the assumption of rotational symmetry -and a constant propagation direction. We have shown that the latter is given for this jet event to some extent. Furthermore, we assume a constant propagation direction and radial dynamic pressure profiles that resemble Gaussian distributions. The problem can thus be reduced to two dimensions. This then gives us the possibility to enables us estimate the perpendicular scale size for different cross sections of a jet. Together with the parallel scale size, we could create a simple 3D model of the magnetosheath jet. To apply this method, it is necessary to observe the flow pattern of the ambient magnetosheath plasma reported-described by Plaschke and Hietala (2018). At least one of the two motions - diverging or converging plasma flow - is required-should be visible to determine the position of the jet center. Thus, this estimation is central axis. Observing

both parts of the vortical motion leads to more reliable results. This estimation is therefore not applicable to all jets observed by multiple spacecraft, as individual events can deviate strongly from the average behavior. As Plaschke et al. (2020b) have shown for the alignment of velocity and magnetic field, the fluctuations can easily be on the same order of magnitude as the average alignment effect. ~~Also in this case study, we don't see a clear diverging flow ahead of the jet-~~

Note that the method described in this paper relies on further above mentioned assumptions and simplifications. ~~We assume rotational symmetry of the dynamic pressure distribution around the central axis that is aligned with the constant propagation direction-~~The choice of the Gaussian distribution for the fit implies a corresponding monotonous decrease of the dynamic pressure from the center towards the edges. ~~Both These~~ assumptions may not ~~be necessarily necessarily be~~ satisfied in general or in some parts of the jet. To perform our analysis we need at least ~~three spacecraft. two spacecraft.~~ However, as evident for this jet event, this is not necessarily sufficient, as the spacecraft should be well separated from each other. More spacecraft observing the same jet or the ambient magnetosheath would allow an evaluation of the validity of our assumptions.

#### 4 Summary and Conclusion

We observed the ~~flow pattern of the ambient plasma due to the passage of~~ vortical motion of plasma within a jet with the three THEMIS spacecraft THA, THD and THE. From the ~~converging plasma flow after jet passage~~ diverging flows ahead of and the converging plasma flows behind the jets maximum dynamic pressure region (at  $t_{\max}$ ) we were able to estimate the position of the jet central axis. The distances of the spacecraft from the central axis were used together with the measured  $P_{\text{dyn},x}$  ~~was used to fit a Gaussian distribution with an additional offset corresponding to the background dynamic pressure. This was shown for~~ to fit Gaussian distributions. This allowed us to determine the dynamic pressure profiles and the perpendicular sizes of the jet within different cross sections.

Here we demonstrate a new method to determine the size for single jet events using in principle measurements from only two spacecraft. In this paper, dynamic pressure profiles for the jet event were presented for three different times ( $t_{\max}-9\text{ s}$ ,  $t_{\max}$  and  $t_{\max}+12\text{ s}$ ) with the following two results:

1. The dynamic pressure in the central part of the jet is higher at  $t_{\max}$  (~~5nPa6 nPa~~) and decreases towards the ~~rear part~~ (3nPa) front and rear parts,
2. The ~~perpendicular size of the jet is larger~~ width of the Gaussian distribution is rather constant over the jet interval. This results in a larger perpendicular size at  $t_{\max}$  (21.2  $R_E$ ) ~~and decreases towards the rear part (1 $R_E$ ) due to the higher dynamic pressure in the center.~~

The apparent larger scale size around  $t_{\max}$  suggests that some spacecraft may only observe central parts of a jet rather than the front and rear parts when passing through edge regions. In addition, spacecraft will unlikely observe the exact center of a jet. Thus, they would measure just a fraction of the dynamic pressure in the jet center (a lower limit) as  $P_{\text{dyn},x}$  decreases towards the edges and this would not necessarily be representative for the jet. This implies that statistical studies of dynamic pressures of jets may significantly and systematically underestimate the maximum values (e.g., Raptis et al., 2020).

305 Finally, the larger expansion near  $t_{\max}$  leads to longer observation times by spacecraft passing the central region of jets. In contrast, the dynamic pressure at the front and rear parts falls below the detection threshold earlier, leading together with the faster decrease of  $P_{\text{dyn},x}$  (corresponds to smaller  $\Delta R$ ) to shorter spacecraft observation times.

The jet event selected for this case study belongs to a small fraction of jet measurements observations that show signs of the expected flow pattern that is needed for the estimation of the center. With only three spacecraft available, there are uncertainties regarding the quality and applicability of the fit and validity of our assumption of rotational symmetry. To increase our confidence in the fit and our assumptions, it would be useful to obtain measurements from even more spacecraft on a jet. This could be achieved through conjunctions of spacecraft from different missions like Cluster, Magnetospheric Multiscale (MMS, Burch et al., 2016) and THEMIS.

### Appendix A: Uncertainty of $V_{\text{jet}}$

315 The propagation direction of the jet ( $V_{\text{jet}}$ ) may have a great impact on our analysis. If the direction is incorrect or poorly determined, it is possible that we do not notice the vortical movement even though it is actually present or vice versa. We estimated  $V_{\text{jet}}$  as a mean value of multiple measurements by THA and THE. Thus, we imply a constant propagation direction over time and that the velocities at both spacecraft positions represent the propagation well. To handle the uncertainty of this assumptions, we take a look at the maximum differences from the mean velocity (cf. Fig. 3). Adding or subtracting these values to/from  $V_{\text{jet}}$  result in  $V_{\text{jet,max}}$  and  $V_{\text{jet,min}}$  as alternative propagation directions.

320 With  $V_{\text{jet,max}}$  and  $V_{\text{jet,min}}$  we can transform the measured ion velocities and the positions of the spacecraft into new coordinate systems using Eq. 2. We then look at the transformed velocities in the  $Y' - Z'$  plane (perpendicular to the propagation direction). This is shown in Fig. A1 for  $V_{\text{jet,max}}$  in the top row, for  $V_{\text{jet,min}}$  in the bottom row and for  $V_{\text{jet}}$  in the middle row (for comparison).

325 We observe the diverging flows before and the converging flows after  $t_{\max}$  in all three cases. In addition, we also investigate if the use of the peak velocities of the 1D VDFs has an influence on our results. Therefore we use the same propagation directions  $V_{\text{jet,max}}$ ,  $V_{\text{jet}}$  and  $V_{\text{jet,min}}$  and transform the ion velocities calculated from the full moments. This is shown in Fig. A2.

330 Although there are some changes, we can again observe in all cases the diverging flows before and the converging flows after  $t_{\max}$ . Thus we conclude that the flow pattern we observe is not an artifact from our data handling.

### Appendix B: Uncertainty of jet center estimation

Since THA and THE are close to each other and in the vicinity of the central axis in the plane perpendicular to the propagation direction, minor deviations of the position of this axis can have major effects on the dynamic pressure profiles. Therefore, we use the maximum differences from the mean to calculate alternative positions of the central axis and compare the resulting pressure profiles. In order to achieve this, we look at the fit parameters  $P_0$  and  $\Delta R$  and how these values change with varying

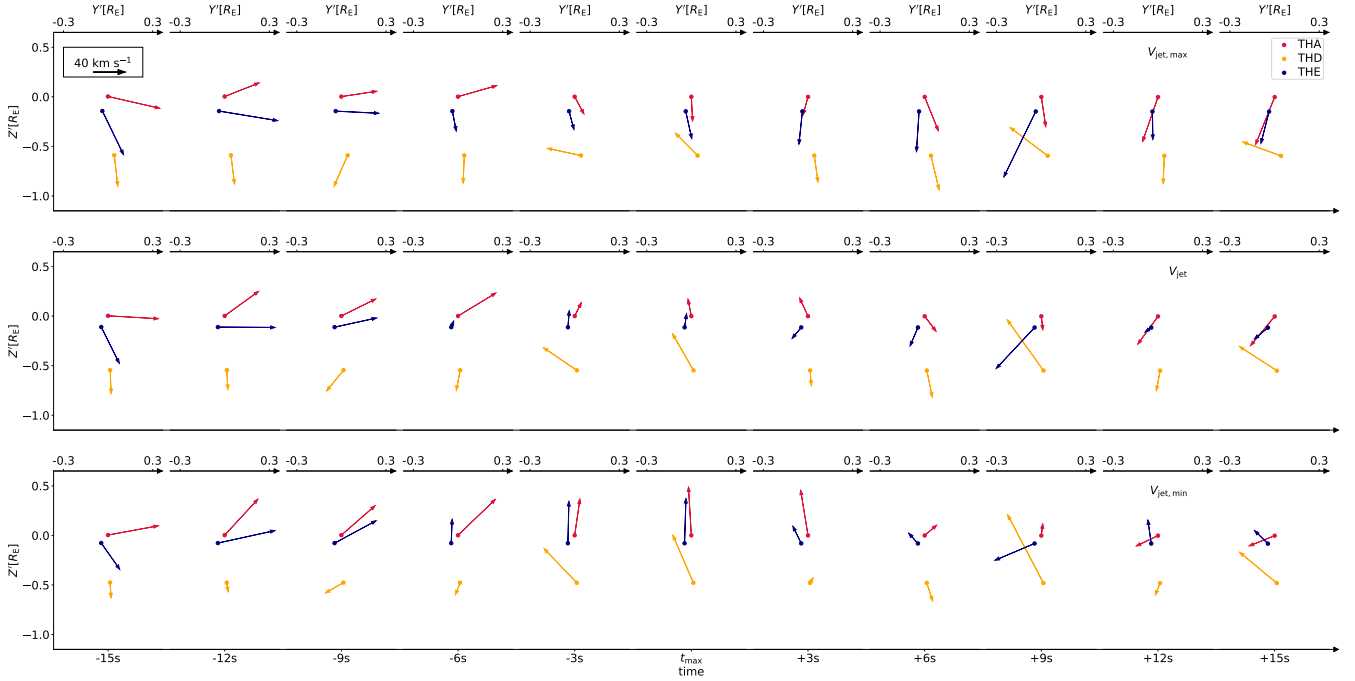


**Figure A1.** Ion velocities from the 1D VDF peaks at the three spacecraft positions for 11 time steps around  $t_{\max}$  in the plane perpendicular to the jet propagation direction. The circles represent the spacecraft positions and the arrows indicate the velocities. The colors for THA, THD, and THE are red, orange, and blue, respectively. The top axes show the corresponding  $Y'$  coordinates for each time step, while the bottom axes display the time steps. In the upper left corner, the black arrow indicates the scale. The top, middle and bottom row were calculated with  $V_{\text{jet,max}}$ ,  $V_{\text{jet}}$  and  $V_{\text{jet,min}}$  as propagation direction, respectively.

central axis positions. In addition, we investigate again whether the use of the peak velocities from the 1D VDFs has a major influence on the results. Therefore, we calculate  $P_{\text{dyn},x}$  from the velocities from the full moments and repeat the comparison. These results are presented in Fig. B1.

340 The panels (from top to bottom) show the time evolution of the fit parameters  $P_0$  (a1,a2) and  $\Delta R$  (b1,b2) and the time evolution of their uncertainties  $\sigma(P_0)$  (c1,c2) and  $\sigma(\Delta R)$  (d1,d2). The left and right column show parameters for the dynamic pressure calculated with the velocities from the 1D VDF peaks and with the velocities from the full moments, respectively. The lines represent the results with the mean central axis (solid) and the mean central axis with errors subtracted/added (dotted/dashed).

345 The dynamic pressure at the central axis is highest around  $t_{\max}$  for all cases. For the subtracted errors we see an additional peak later at  $t_{\max}+12\text{s}$ . Looking at Fig. B1c, we can see that the uncertainty of the fit parameter  $\sigma(P_0)$  is higher when we subtract the errors as it reduces the inter spacecraft distances.

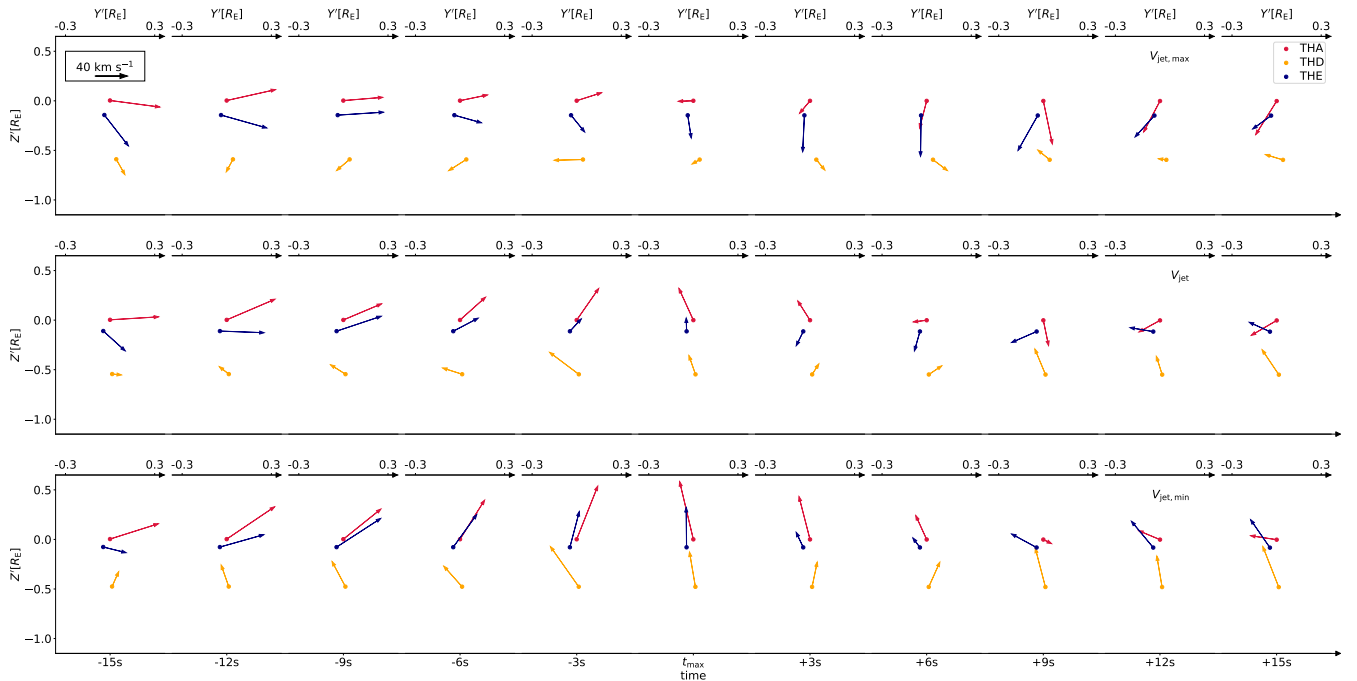


**Figure A2.** Ion velocities from the full moments at the three spacecraft positions for 11 time steps around  $t_{\max}$  in the plane perpendicular to the jet propagation direction. The circles represent the spacecraft positions and the arrows indicate the velocities. The colors for THA, THD, and THE are red, orange, and blue, respectively. The top axes show the corresponding  $Y'$  coordinates for each time step, while the bottom axes display the time steps. In the upper left corner, the black arrow indicates the scale. The top, middle and bottom row were calculated with  $V_{\text{jet,max}}$ ,  $V_{\text{jet}}$  and  $V_{\text{jet,min}}$  as propagation direction, respectively.

For  $\Delta R$  (Fig. B1c) we observe again a rather constant value over the whole time with some exceptions that correlate well with higher uncertainties in  $\sigma(\Delta R)$  (Fig. B1d). These extremely high uncertainties arise when the data do not show a monotonic decrease in dynamic pressure and a Gaussian fit is not appropriate.

350 Apart from outliers, corresponding to high uncertainties, we observe the same behavior for the fit parameters in all cases. Therefore, we argue that the exact position of the central axis does not have a major impact on our conclusion.

*Data availability.* Data from the THEMIS mission including level 2 FGM and ESA data are publicly available from the University of California Berkeley and can be obtained from <http://themis.ssl.berkeley.edu/data/themis> (THEMIS, 2023). The solar wind data from NASA's OMNI high-resolution data set (1 min cadence) are also publicly available and can be obtained from [https://spdf.gsfc.nasa.gov/pub/data/omni/omni\\_cdaweb](https://spdf.gsfc.nasa.gov/pub/data/omni/omni_cdaweb) (OMNI, 2023). THEMIS and OMNI data were accessed using the PySPEDAS software (Grimes et al., 2018; Angelopoulos et al., 2019).



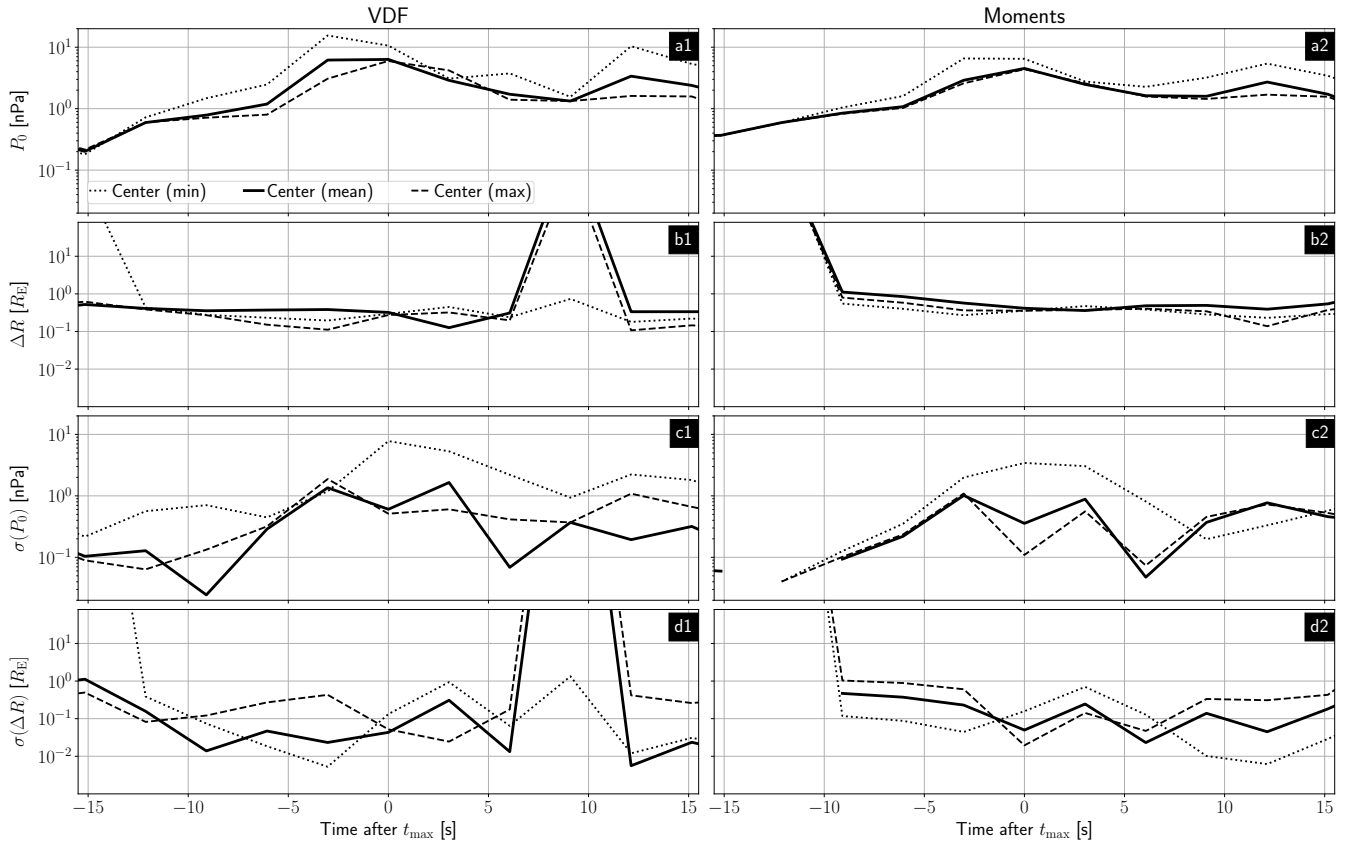


**Figure B1.** The lines represent the results with the mean central axis (solid), mean central axis with errors subtracted (dotted) and errors added (dashed). The left and right column show parameters for the dynamic pressure calculated with the velocities from the 1D VDF peaks and with the velocities from the full moments, respectively. The panels from top to bottom show the time evolution of the fit parameters  $P_0$  (a1,a2) and  $\Delta R$  (b1,b2) and the time evolution of their uncertainties  $\sigma(P_0)$  (c1,c2) and  $\sigma(\Delta R)$  (d1,d2).

*Author contributions.* AP performed the main work. GG, FK, TK, ZV and FP helped with the discussions and interpretations of the results. JM took care of THEMIS FGM calibrations and brought his expertise on THEMIS data into the discussions.

*Competing interests.* The authors declare that they have no conflict of interest.

360 *Acknowledgements.* We acknowledge NASA contract NAS5-02099 for use of data from the THEMIS Mission, specifically C.W. Carlson and J. P. McFadden for the use of ESA data; K. H. Glassmeier, U. Auster, and W. Baumjohann for the use of FGM data provided under the lead of the Technical University of Braunschweig and with financial support through the German Ministry for Economy and Technology and the German Center for Aviation and Space (DLR) under contract 50 OC 0302. This work was financially supported by the German Center

for Aviation and Space (DLR) under contract 50 OC 2201. FK and ZV acknowledge the support by the Austrian Science Fund (FWF), P  
365 33285-N.

## References

- Angelopoulos, V.: The THEMIS Mission, *Space Sci. Rev.*, 141, 5–34, <https://doi.org/10.1007/s11214-008-9336-1>, 2008.
- Angelopoulos, V., Cruce, P., Drozdov, A., Grimes, E. W., Hatzigeorgiu, N., King, D. A., et al.: The Space Physics Environment Data Analysis System (SPEDAS), *Space Sci. Rev.*, 215, 9, <https://doi.org/10.1007/s11214-018-0576-4>, 2019.
- 370 Archer, M. O., Horbury, T. S., and Eastwood, J. P.: Magnetosheath pressure pulses: Generation downstream of the bow shock from solar wind discontinuities, *J. Geophys. Res.-Space*, 117, <https://doi.org/https://doi.org/10.1029/2011JA017468>, 2012.
- Archer, M. O., Hietala, H., Hartinger, M. D., Plaschke, F., and Angelopoulos, V.: Direct observations of a surface eigenmode of the dayside magnetopause, *Nat. Commun.*, 10, <https://doi.org/10.1038/s41467-018-08134-5>, 2019.
- Auster, H., Glassmeier, K., Magnes, W., and W. Baumjohann, O. A., Constantinescu, D., Fischer, D., Fornacon, K., Georgescu, E., Harvey, P., Hillenmaier, O., Kroth, R., Ludlam, M., Narita, Y., Nakamura, R., Okrafka, K., Plaschke, F., Richter, I., Schwarzl, H., Stoll, B., Valavanoglou, A., and Wiedemann, M.: The THEMIS Fluxgate Magnetometer, *Space Sci. Rev.*, 141, 235–264, <https://doi.org/10.1007/s11214-008-9365-9>, 2008.
- 375 Balogh, A., Schwartz, S. J., Bale, S. D., Balikhin, M. A., Burgess, D., Horbury, T. S., Krasnoselskikh, V. V., Kucharek, H., Lembège, B., Lucek, E. A., Möbius, E., Scholer, M., Thomsen, M. F., and Walker, S. N.: Cluster at the Bow Shock: Introduction, *Space Sci. Rev.*, 118, 155–160, <https://doi.org/10.1007/s11214-005-3826-1>, 2005.
- 380 Burch, J. L. and Moore, T. E., Torbert, R. B., and Giles, B. L.: Magnetospheric Multiscale Overview and Science Objectives, *Space Sci. Rev.*, 199, 5–21, <https://doi.org/10.1007/s11214-015-0164-9>, 2016.
- Dmitriev, A. V. and Suvorova, A. V.: Large-scale jets in the magnetosheath and plasma penetration across the magnetopause: THEMIS observations, *J. Geophys. Res.-Space*, 120, 4423–4437, <https://doi.org/https://doi.org/10.1002/2014JA020953>, 2015.
- 385 Dmitriev, A. V. and Suvorova, A. V.: Atmospheric Effects of Magnetosheath Jets, *Atmosphere*, 14, <https://doi.org/10.3390/atmos14010045>, 2023.
- Eastwood, J. P., Lucek, E. A., Mazelle, C., Meziane, K., Narita, Y., Pickett, J., and Treumann, R. A.: The Foreshock, *Space Sci. Rev.*, 118, 41–94, <https://doi.org/10.1007/s11214-005-3824-3>, 2005.
- Escoubet, C., Fehringer, M., and Goldstein, M.: The Cluster mission, *Ann. Geophys.*, 19, 1197–1200, <https://doi.org/10.5194/angeo-19-1197-2001>, 2001.
- 390 Grimes, E. W., Lewis, J. W., Angelopoulos, V., McTiernan, J. M., Hatzigeorgiu, N., Drozdov, A., and Russell, C.: Pyspedas, a Python Implementation of SPEDAS, in: AGU Fall Meeting Abstracts, vol. 2018, pp. IN11B–0629, 2018.
- Gunell, H., Stenberg Wieser, G., Mella, M., Maggiolo, R., Nilsson, H., Darrouzet, F., Hamrin, M., Karlsson, T., Brenning, N., De Keyser, J., André, M., and Dandouras, I.: Waves in high-speed plasmoids in the magnetosheath and at the magnetopause, *Ann. Geophys.*, 32, 991–1009, <https://doi.org/10.5194/angeo-32-991-2014>, 2014.
- 395 Han, D.-S., Hietala, H., Chen, X.-C., Nishimura, Y., Lyons, L. R., Liu, J.-J., Hu, H.-Q., and Yang, H.-G.: Observational properties of dayside throat aurora and implications on the possible generation mechanisms, *J. Geophys. Res.-Space*, 122, 1853–1870, <https://doi.org/https://doi.org/10.1002/2016JA023394>, 2017.
- Hietala, H., Laitinen, T. V., Andréová, K., Vainio, R., Vaivads, A., Palmroth, M., Pulkkinen, T. I., Koskinen, H. E. J., Lucek, E. A., and Rème, H.: Supermagnetosonic Jets behind a Collisionless Quasiparallel Shock, *Phys. Rev. Lett.*, 103, 245 001, <https://doi.org/10.1103/PhysRevLett.103.245001>, 2009.
- 400

- Hietala, H., Partamies, N., Laitinen, T. V., Clausen, L. B. N., Facskó, G., Vaivads, A., Koskinen, H. E. J., Dandouras, I., Rème, H., and Lucek, E. A.: Supermagnetosonic subsolar magnetosheath jets and their effects: from the solar wind to the ionospheric convection, *Ann. Geophys.*, 30, 33–48, <https://doi.org/10.5194/angeo-30-33-2012>, 2012.
- 405 Hietala, H., Phan, T. D., Angelopoulos, V., Oieroset, M., Archer, M. O., Karlsson, T., and Plaschke, F.: In Situ Observations of a Magnetosheath High-Speed Jet Triggering Magnetopause Reconnection, *Geophys. Res. Lett.*, 45, 1732–1740, <https://doi.org/https://doi.org/10.1002/2017GL076525>, 2018.
- Karlsson, T., Brenning, N., Nilsson, H., Trotignon, J.-G., Vallières, X., and Facsko, G.: Localized density enhancements in the magnetosheath: Three-dimensional morphology and possible importance for impulsive penetration, *J. Geophys. Res.-Space*, 117, <https://doi.org/https://doi.org/10.1029/2011JA017059>, 2012.
- 410 Karlsson, T., Plaschke, F., Hietala, H., Archer, M., Blanco-Cano, X., Kajdič, P., Lindqvist, P.-A., Marklund, G., and Gershman, D. J.: Investigating the anatomy of magnetosheath jets – MMS observations, *Ann. Geophys.*, 36, 655–677, <https://doi.org/10.5194/angeo-36-655-2018>, 2018.
- King, J. H. and Papitashvili, N. E.: Solar wind spatial scales in and comparisons of hourly Wind and ACE plasma and magnetic field data, *J. Geophys. Res.-Space*, 110, <https://doi.org/https://doi.org/10.1029/2004JA010649>, 2005.
- 415 Koller, F., Plaschke, F., Temmer, M., Preisser, L., Roberts, O. W., and Vörös, Z.: Magnetosheath Jet Formation Influenced by Parameters in Solar Wind Structures, *J. Geophys. Res.-Space*, 128, e2023JA031339, <https://doi.org/https://doi.org/10.1029/2023JA031339>, 2023.
- LaMoury, A. T., Hietala, H., Plaschke, F., Vuorinen, L., and Eastwood, J. P.: Solar Wind Control of Magnetosheath Jet Formation and Propagation to the Magnetopause, *J. Geophys. Res.-Space*, 126, e2021JA029592, <https://doi.org/https://doi.org/10.1029/2021JA029592>, <https://doi.org/https://doi.org/10.1029/2021JA029592>, 2021.
- 420 McFadden, J., Carlson, C., Larson, D., Ludlam, M., Abiad, R., Elliott, B., Turin, P., Marckwordt, M., and Angelopoulos, V.: The THEMIS ESA Plasma Instrument and In-flight Calibration, *Space Sci. Rev.*, 141, 277–302, <https://doi.org/10.1007/s11214-008-9440-2>, 2008.
- Němeček, Z., Šafránková, J., Přeč, L., Sibeck, D. G., Kokubun, S., and Mukai, T.: Transient flux enhancements in the magnetosheath, *Geophys. Res. Lett.*, 25, 1273–1276, <https://doi.org/https://doi.org/10.1029/98GL50873>, 1998.
- 425 Nykyri, K., Bengtson, M., Angelopoulos, V., Nishimura, Y., and Wing, S.: Can Enhanced Flux Loading by High-Speed Jets Lead to a Substorm? Multipoint Detection of the Christmas Day Substorm Onset at 08:17 UT, 2015, *J. Geophys. Res.-Space*, 124, 4314–4340, <https://doi.org/https://doi.org/10.1029/2018JA026357>, 2019.
- OMNI: Solar wind data from NASA's OMNI high resolution data set, available at: [https://omniweb.gsfc.nasa.gov/ow\\_min.html](https://omniweb.gsfc.nasa.gov/ow_min.html), last access: 21 December 2023, 2023.
- 430 Palmroth, M., Raptis, S., Suni, J., Karlsson, T., Turc, L., Johlander, A., Ganse, U., Pfau-Kempf, Y., Blanco-Cano, X., Akhavan-Tafti, M., Battarbee, M., Dubart, M., Grandin, M., Tarvus, V., and Osmane, A.: Magnetosheath jet evolution as a function of lifetime: global hybrid-Vlasov simulations compared to MMS observations, *Ann. Geophys.*, 39, 289–308, <https://doi.org/10.5194/angeo-39-289-2021>, 2021.
- Plaschke, F. and Hietala, H.: Plasma flow patterns in and around magnetosheath jets, *Ann. Geophys.*, 36, 695–703, <https://doi.org/10.5194/angeo-36-695-2018>, 2018.
- 435 Plaschke, F., Hietala, H., and Angelopoulos, V.: Anti-sunward high-speed jets in the subsolar magnetosheath, *Ann. Geophys.*, 31, 1877–1889, <https://doi.org/10.5194/angeo-31-1877-2013>, 2013.
- Plaschke, F., Hietala, H., Angelopoulos, V., and Nakamura, R.: Geoeffective jets impacting the magnetopause are very common, *J. Geophys. Res.-Space*, 121, 3240–3253, <https://doi.org/https://doi.org/10.1002/2016JA022534>, 2016.

- 440 Plaschke, F., Karlsson, T., Hietala, H., Archer, M., Vörös, Z., Nakamura, R., Magnes, W., Baumjohann, W., Torbert, R. B., Russell, C. T., and Giles, B. L.: Magnetosheath High-Speed Jets: Internal Structure and Interaction With Ambient Plasma, *J. Geophys. Res.-Space*, 122, 10,157–10,175, <https://doi.org/https://doi.org/10.1002/2017JA024471>, 2017.
- Plaschke, F., Hietala, H., Archer, M. O., Blanco-Cano, X., Kajdič, P., Karlsson, T., Lee, S. H., Omidi, N., Palmroth, M., Roytershteyn, V., Schmid, D., Sergeev, V., and Sibeck, D.: Jets Downstream of Collisionless Shocks, *Space Sci. Rev.*, 214, <https://doi.org/10.1007/s11214-018-0516-3>, 2018.
- 445 Plaschke, F., Hietala, H., and Vörös, Z.: Scale Sizes of Magnetosheath Jets, *J. Geophys. Res.-Space*, 125, e2020JA027962, <https://doi.org/https://doi.org/10.1029/2020JA027962>, 2020a.
- Plaschke, F., Jernej, M., Hietala, H., and Vuorinen, L.: On the alignment of velocity and magnetic fields within magnetosheath jets, *Ann. Geophys.*, 38, 287–296, <https://doi.org/10.5194/angeo-38-287-2020>, 2020b.
- Raptis, S., Karlsson, T., Plaschke, F., Kullen, A., and Lindqvist, P.-A.: Classifying Magnetosheath Jets Using MMS: Statistical Properties, *J. Geophys. Res.-Space*, 125, e2019JA027754, <https://doi.org/https://doi.org/10.1029/2019JA027754>, e2019JA027754 10.1029/2019JA027754, 2020.
- 450 Raptis, S., Karlsson, T., Vaivads, A., Lindberg, M., Johlander, A., and Trollvik, H.: On Magnetosheath Jet Kinetic Structure and Plasma Properties, *Geophysical Research Letters*, 49, e2022GL100678, <https://doi.org/https://doi.org/10.1029/2022GL100678>, e2022GL100678 2022GL100678, 2022a.
- 455 Raptis, S., Karlsson, T., Vaivads, A., Pollock, C., Plaschke, F., Johlander, A., Trollvik, H., and Lindqvist, P.-A.: Downstream high-speed plasma jet generation as a direct consequence of shock reformation, *Nat. Commun.*, 13, 598, <https://doi.org/10.1038/s41467-022-28110-4>, 2022b.
- Savin, S., Amata, E., Zelenyi, L., Lutsenko, V., Safrankova, J., Nemecek, Z., Borodkova, N., Buechner, J., Daly, P. W., Kronberg, E. A., Blecki, J., Budaev, V., Kozak, L., Skalsky, A., and Lezhen, L.: Super fast plasma streams as drivers of transient and anomalous magnetospheric dynamics, *Ann. Geophys.*, 30, 1–7, <https://doi.org/10.5194/angeo-30-1-2012>, 2012.
- 460 Schwartz, S. J. and Burgess, D.: Quasi-parallel shocks: A patchwork of three-dimensional structures, *Geophys. Res. Lett.*, 18, 373–376, <https://doi.org/https://doi.org/10.1029/91GL00138>, 1991.
- Shue, J.-H., Chao, J.-K., Song, P., McFadden, J. P., Suvorova, A., Angelopoulos, V., Glassmeier, K. H., and Plaschke, F.: Anomalous magnetosheath flows and distorted subsolar magnetopause for radial interplanetary magnetic fields, *Geophys. Res. Lett.*, 36, <https://doi.org/https://doi.org/10.1029/2009GL039842>, 2009.
- 465 Spreiter, J. R., Summers, A. L., and Alksne, A. Y.: Hydromagnetic flow around the magnetosphere, *Planet. Space Sci.*, 14, 223–253, [https://doi.org/https://doi.org/10.1016/0032-0633\(66\)90124-3](https://doi.org/https://doi.org/10.1016/0032-0633(66)90124-3), 1966.
- Suni, J., Palmroth, M., Turc, L., Battarbee, M., Johlander, A., Taurus, V., Alho, M., Bussov, M., Dubart, M., Ganse, U., Grandin, M., Horaites, K., Manglayev, T., Papadakis, K., Pfau-Kempf, Y., and Zhou, H.: Connection Between Foreshock Structures and the Generation of Magnetosheath Jets: Vlasiator Results, *Geophys. Res. Lett.*, 48, e2021GL095655, <https://doi.org/https://doi.org/10.1029/2021GL095655>, 2021.
- 470 THEMIS: THEMIS mission including level 2 FGM and ESA data, available at: <http://themis.ssl.berkeley.edu/data/themis>, last access: 21 December 2023, 2023.
- Vuorinen, L., Hietala, H., and Plaschke, F.: Jets in the magnetosheath: IMF control of where they occur, *Ann. Geophys.*, 37, 689–697, <https://doi.org/10.5194/angeo-37-689-2019>, 2019.
- 475

Vuorinen, L., Hietala, H., Plaschke, F., and LaMoury, A. T.: Magnetic Field in Magnetosheath Jets: A Statistical Study of BZ Near the Magnetopause, *Journal of Geophysical Research: Space Physics*, 126, e2021JA029188, <https://doi.org/https://doi.org/10.1029/2021JA029188>, 2021.